Unsteady Far-Field Drag Analyses of Transonic Buffet over the NASA Common Research Model

Camille Fournis, Ilias Petropoulos, Fulvio Sartor

Association Aéronautique et Astronautique de France

57th 3AF International Conference on Applied Aerodynamics
29 — 31 March 2023, Bordeaux – France

AERO2023-24

Unsteady Far-Field Drag Analyses of Transonic Buffet over the NASA Common Research Model

Camille Fournis[(1)], Ilias Petropoulos[(1)] and Fulvio Sartor[(1)]

[(1)]ONERA, 8 rue des Vertugadins 92190 Meudon, France, corresponding author: camille.fournis@onera.fr

ABSTRACT

This paper presents an analysis of the physics of transonic buffet by means of phenomenological far-field decomposition of drag. The analysis relies on the unsteady far-field drag decomposition developed by Toubin et al. ("Improved Unsteady Far-Field Drag Breakdown Method and Application to Complex Cases," *AIAA Journal*, Vol. 54, No. 6, 2016) so far applied to pitching airfoils and wings, vortex-shedding and two-dimensional transonic buffet. It provides a decomposition of drag into viscous, wave, lift-induced and acoustic components. First of all, the formulation of Toubin et al. is presented and a physical interpretation of the terms of the decomposition is given. Then, the main buffet characteristics are shown on the wing-body configuration of the NASA Common Research Model[1] (CRM) investigated in the frame of the 7th AIAA Drag Prediction Workshop (DPW-7). Later on, the unsteady drag exerted on the aircraft is decomposed and the evolution of the various drag components over time is investigated.

INTRODUCTION

Given the inevitable economical and environmental challenges that have to be addressed, the aviation sector is ever more keen on reducing its operating costs and carbon footprint. One big aspect of this task is to minimize the fuel consumption of aircraft.

That is why accurate drag prediction has always been of paramount importance when designing an aircraft. Indeed, fuel consumption is a direct consequence of the amount of drag exerted on the aircraft, hence drag reduction implies lower fuel consumption. But before reducing drag, it is necessary to accurately measure and quantify it. To do so, multiple scientists have been developing drag prediction methods throughout the twentieth century. Some of those methods rely on the far-field approach, which consists in considering the momentum balance in a control volume of fluid surrounding the aircraft. It differs from the classical near-field (nf) approach, which mechanically decomposes drag into pressure and friction components on the aircraft skin:

$$D_{nf} = D_p + D_f = \oint_{S_a} (p - p_\infty)\, n_x \, \mathrm{d}S - \oint_{S_a} \tau_x \cdot \mathbf{n} \, \mathrm{d}S \quad (1)$$

Indeed, the far-field (ff) approach traditionally decomposes drag into phenomenological contributions: lift-induced drag D_i, viscous drag D_v and wave drag D_w.

$$D_{ff} = D_i + D_v + D_w \quad (2)$$

This breakdown is crucial for aircraft designers because it provides an insight on the physical sources of drag and helps to identify a potential for the improvement of the aircraft geometry.

The lift-induced drag was first identified at the beginning of the twentieth century by Prandtl in his famous lifting-line theory [14] and its definition was amended in the seventies by Maskell [9]. Methods for viscous and wave drag computation were then defined using thermodynamic approaches introduced by Oswatitsch [12] in 1945 and later by van der Vooren and Sloof [20] in the nineties. In further developments, Destarac and van der Vooren [3, 4] defined the lift-induced drag indirectly, by merely subtracting the irreversible drag (viscous plus wave drag) from the total far-field drag. In spite of the insights provided by those developments, these drag prediction and decomposition methods were only applicable to steady flows.

In the recent years, several formulations aimed at assessing and decomposing drag in unsteady flows have been developed [5, 10, 11, 18, 19]. Gariépy et al. [5] were the first to propose a generalization of the Destarac-van

[1]CRM website: http://commonresearchmodel.larc.nasa.gov/

der Vooren approach [3, 4] in unsteady flows. However, as shown by Toubin and Bailly [18], their decomposition is very sensitive to the size of the control volumes used for the integration of the various drag components: an extension of the integration volumes in the wake creates an unphysical phase shift on the time evolution of the far-field drag components.

Indeed, it is necessary that the phase of all far-field drag components be invariant to the size of the integration domain, in order to guarantee an objective physical unsteady drag breakdown. Moreover, it ensures that the far-field drag integrated in the flowfield surrounding the aircraft (hence comprising all the unsteady phenomena occuring therein) is consistent at all times with the near-field drag integrated on the skin of the aircraft. This particular aspect has been one of the major successes of Toubin's doctoral thesis [17]. Toubin et al. [17, 18, 19] developed an unsteady drag breakdown based on the Destarac-van der Vooren formulation [4]. They validated this method on a number of academic cases and demonstrated its robustness with respect to the integration volume extension in the wake.

The interest in unsteady phenomenological drag breakdown has so far been limited to relatively academic cases. Recent drag-related studies have however begun to emerge on the more applied NASA CRM aircraft in transonic buffet conditions. Steady investigations of the CRM have been the main focus of recent AIAA Drag Prediction Workshops (DPWs) [2, 16]. As an extension of these studies, the latest edition (DPW-7) featured a task dedicated to "Beyond RANS" analyses, aiming at investigating flight conditions at greater Reynolds numbers and higher angles of attack. ONERA took part in this DPW-7 task on the basis of unsteady Reynolds-averaged Navier-Stokes (URANS) computations. In particular, when considering a wing in cruise conditions and increasing the angle of attack, periodic shockwave motions known as transonic buffet occur, and the flow is unsteady [8]. The unsteadiness predominantly consists of a periodic self-sustained motion of the shock as well as unsteady separation of the boundary layer, consequences in the flowfield that will be analyzed in the present work.

The aim of this study is to investigate whether an unsteady drag decomposition can establish links between the evolution of drag components and unsteady phenomena occurring within the flow field. This work has been carried out by using the far-field decomposition of Toubin et al. [19] to analyze URANS computations of the DPW-7 CRM configuration in transonic buffet regime. The study is structured as follows. The formulation employed is first presented in Section 1, followed by Section 2 which gives an overview of ONERA computational studies of buffet prediction in the frame of the DPW-7. Finally, Section 3 presents investigations on the unsteady drag breakdown of the CRM case.

1. PRESENTATION OF THE UNSTEADY FAR-FIELD DRAG DECOMPOSITION OF TOUBIN ET AL.

1.1 Original formulation

To overcome the phase shift issue raised by the formulation of Gariépy et al. [5], Toubin and Bailly [18] adopted a different approach, based on a drag balance in streamtubes, in order to account for the time delay and propagation of flow perturbations created at the source of drag by shockwave motion, vortex-shedding or a pitching airfoil or wing for instance. By doing so, they could eliminate the phase shift entailed by an extension of the control volumes in the wake. Their formulation is presented below:

$$D_{ff} = D_w + D_v + D_{ui} + D_m \tag{3}$$

with:

$$D_w = -\oint_{S_w} \rho\left(U_{\text{irr}} - U_\infty\right)(\mathbf{q}\cdot\mathbf{n})\,\mathrm{d}S - \int_{V_w} \frac{\partial \rho\left(U-U_\infty\right)}{\partial t}\mathrm{d}V - \int_{V_{wd}} \left(\frac{\partial \rho\left(U-U_{\text{irr}}\right)}{\partial t} + \frac{1}{U_{\text{irr}}}\frac{\partial p}{\partial t}\right)\mathrm{d}V \tag{4}$$

$$D_v = \oint_{S_v} \left(-\rho\left(U_{\text{irr}} - U_\infty\right)\mathbf{q} + \tau_x\right)\cdot\mathbf{n}\,\mathrm{d}S - \int_{V_v} \frac{\partial \rho\left(U-U_\infty\right)}{\partial t}\mathrm{d}V \tag{5}$$

$$D_{ui} = \oint_{S_e} \left(-\rho\left(U-U_{\text{irr}}\right)\mathbf{q} - \left(p-p_\infty\right)\mathbf{e}_x\right)\cdot\mathbf{n}\,\mathrm{d}S - \int_{V_c} \left(\frac{\partial \rho\left(U-U_{\text{irr}}\right)}{\partial t} + \frac{1}{U_{\text{irr}}}\frac{\partial p}{\partial t}\right)\mathrm{d}V \tag{6}$$

$$D_m = -\oint_{S_a} \rho\left(U-U_\infty\right)(\mathbf{q}\cdot\mathbf{n})\,\mathrm{d}S \tag{7}$$

where D_{ui} is the unsteady lift-induced drag and D_m is the drag generated by solid body motion, henceforth referred to as motion drag. The volumes and surfaces are illustrated in Fig. 1 and S_a is the skin surface of the aircraft. Here $\mathbf{q}$ is the velocity vector, $\tau_x = \tau\cdot\mathbf{e}_x$ and U_{irr} is the irreversible axial velocity defect [3, 4] defined by:

$$U_{\text{irr}} = U_\infty\sqrt{1 + \frac{2\Delta H}{U_\infty^2} - \frac{2}{(\gamma-1)M_\infty^2}\left(\mathrm{e}^{\Delta s/C_p} - 1\right)} \tag{8}$$

and $H = C_pT + q^2/2$ is the specific stagnation enthalpy, $\Delta H = H - H_\infty$ is the specific stagnation enthalpy variation, γ is the ratio of specific heats, C_p is the specific heat at constant pressure, and $\Delta s = s - s_\infty$ is the specific entropy variation.

Later on, Toubin et al. [19] further decomposed D_{ui} into an acoustic propagation drag D_{pa} and the lift-induced drag D_i as follows:

$$D_{ui} = D_i + D_{pa} \tag{9}$$

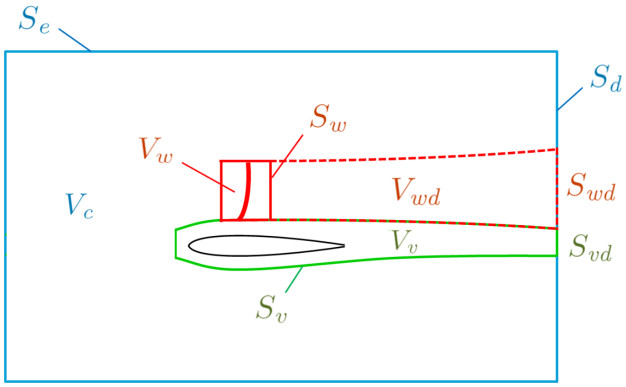

Figure 1: Control volumes used in the integration of the various drag components (from [19])

with:

$$D_i = \oint_{S_e} \left(-\rho\left(U-U_{\text{irr}}\right)\mathbf{q} - \left(p-p_\infty\right)\mathbf{e}_x\right)\cdot\mathbf{n}\,\mathrm{d}S + \int_{V_c} \rho\left(U-U_{\text{irr}}\right)\left(\frac{1}{a}+\frac{1}{U_{\text{irr}}}\right)\frac{\partial U}{\partial t}\mathrm{d}V \tag{10}$$

$$D_{pa} = -\int_{V_c} \frac{\rho\left(U-U_{\text{irr}}\right)}{a}\frac{\partial R^+}{\partial t}\mathrm{d}V \tag{11}$$

where a is the speed of sound and $R^+ = U + 2a/(\gamma-1)$ is the Riemann invariant on characteristic curves of the (x,t) plane defined by $\mathrm{d}x/\mathrm{d}t = U+a$.

In summary, the unsteady far-field drag can be decomposed into five contributions:

$$D_{ff} = D_w + D_v + D_i + D_{pa} + D_m \tag{12}$$

First of all, it is important to note that each drag component includes an unsteady contribution in the formulation of Toubin et al. [19], whereas in the formulation of Gariépy et al. [5], unsteady effects are grouped into a single unsteady drag component. Secondly, in steady flows, all the time derivatives vanish and D_w, D_v and D_i recover their steady expressions given in [3, 4], while D_{pa} is eliminated. Moreover, D_m also disappears in steady regime given the impermeable wall condition $\mathbf{q}\cdot\mathbf{n} = 0$ which holds for both viscous and inviscid flows.

1.2 Single-vector formulation

In the frame of this work, a different but mathematically equivalent formulation has been derived in order to establish an unsteady counterpart of the single-vector version of the steady formulation of Destarac [3]. The derivations rely on the following property in unsteady regime:

$$\nabla\cdot\mathbf{f} = \frac{\partial\rho\left(U-U_\infty\right)}{\partial t} \tag{13}$$

with:

$$\mathbf{f} = -\rho\left(U-U_\infty\right)\mathbf{q} - \left(p-p_\infty\right)\mathbf{e}_x + \tau_x \tag{14}$$

By merely decomposing $\mathbf{f}$ as:

$$\mathbf{f} = \mathbf{f}^*_{vw} + \mathbf{f}^*_i \tag{15}$$

with:

$$\mathbf{f}^*_{vw} = -\rho\left(U_{\text{irr}}-U_\infty\right)\mathbf{q} + \tau_x \tag{16}$$

$$\mathbf{f}^*_i = -\rho\left(U-U_{\text{irr}}\right)\mathbf{q} - \left(p-p_\infty\right)\mathbf{e}_x \tag{17}$$

and after some algebraic manipulations, it is possible to re-express D_w, D_v, D_{ui} and D_i using only the $\mathbf{f}^*_i$ vector:

$$D_w = -\int_{V_{wd}}\left(\frac{\partial\rho\left(U-U_{\text{irr}}\right)}{\partial t} + \frac{1}{U_{\text{irr}}}\frac{\partial p}{\partial t}\right)\mathrm{d}V - \oint_{S_w}\mathbf{f}^*_i\cdot\mathbf{n}\,\mathrm{d}S \tag{18}$$

$$D_v = -\oint_{S_v}\mathbf{f}^*_i\cdot\mathbf{n}\,\mathrm{d}S - D_m + D_{nf} \tag{19}$$

$$D_{ui} = -\int_{V_c}\left(\frac{\partial\rho\left(U-U_{\text{irr}}\right)}{\partial t} + \frac{1}{U_{\text{irr}}}\frac{\partial p}{\partial t}\right)\mathrm{d}V + \oint_{S_e}\mathbf{f}^*_i\cdot\mathbf{n}\,\mathrm{d}S \tag{20}$$

$$D_i = \int_{V_c}\rho\left(U-U_{\text{irr}}\right)\left(\frac{1}{a}+\frac{1}{U_{\text{irr}}}\right)\frac{\partial U}{\partial t}\mathrm{d}V + \oint_{S_e}\mathbf{f}^*_i\cdot\mathbf{n}\,\mathrm{d}S \tag{21}$$

The following far-field drag results have all been obtained by post-processing the CFD solutions with the latter single-vector formulation.

2. ANALYSIS OF THE MAIN BUFFET CHARACTERISTICS ON THE NASA CRM

This section is devoted to the presentation and analysis of the main features of the buffet phenomenon predicted by URANS computations. They were performed using the ONERA-SAFRAN elsA solver [1], in which the turbulence was modeled using the Spalart-Allmaras model [15], and the space discretization was done using the Jameson-Schmidt-Turkel numerical scheme for the convective flux [7]. The time algorithm chosen is Gear, providing a global time stepping.

Those time-accurate simulations correspond to the work carried out by ONERA [6] as part of the "Beyond RANS" optional test-case of the DPW-7. The participants were invited to use alternative methods to analyze a flow at $M_\infty = 0.85$, with high angle of attack ($\alpha = 4°$ and $4.25°$) and possibly buffet phenomenon for a Reynolds number of 20 million over the NASA CRM (the geometry is shown in Fig. 2). ONERA opted for URANS simulations since this approach can provide an accurate description of the unsteadiness of the shockwave while keeping the cost of the simulation reasonable. Contrary to

high-fidelity methods such as DNS or ZDES, URANS is able to provide useful information about the unsteady dynamics of the flow in buffet conditions in a short amount of time and with limited resources. However, the turbulence remains completely modeled as for the steady-state RANS simulations and only the large-scale unsteadiness can be reproduced.

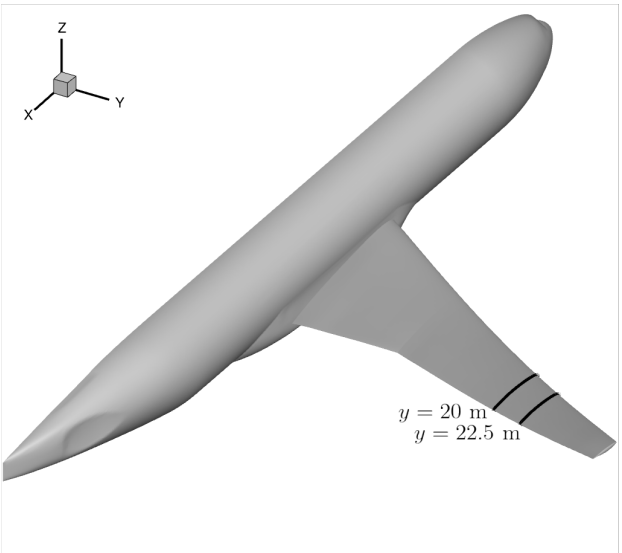

Figure 2: Geometry of the NASA CRM.

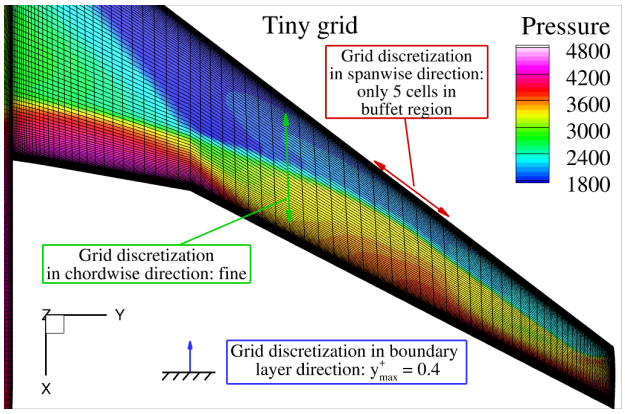

Figure 3: Pressure contour on the wing (Tiny grid).

The choice of the time step is the first question that has been addressed. A convergence study was carried out, starting from the converged RANS solution, using different time steps. At the beginning, the Tiny grid level of the DPW-7 (5M points) was used in order to have a quick estimation of the buffet phenomenon, localize the position of the unsteadiness on the wing, its intensity and, most importantly, the buffet period. While the $y^+ = 0.4$ discretization is sufficiently fine and the buffet phenomenon could be reproduced with shockwave motions observed on the wing, the spanwise spatial discretization in the buffet region is too coarse to validate the result when compared to the Coarse grid (17M points) and the Medium grid (41M points), as depicted in Figs. 3 and 4. According to the data obtained with the Tiny grid, the buffet phenomenon has a frequency of 5.90 Hz (see Fig. 5). For this case, a time step of $\Delta t = 10^{-4}$ s, corresponding to 1700 steps per buffet period, was sufficient to reproduce the phenomenon. Thus, it was concluded that the Tiny grid can reproduce the main features of buffet, despite poor spanwise discretization, but the unsteady behavior of the shockwave might not be correctly captured. Hence the Medium grid has been considered in the following studies. For this grid level, the time step is $\Delta t = 5 \times 10^{-5}$ s, corresponding to roughly 1600 steps per period, with each step converged during 8 inner iterations.

The three images in Fig. 6 present a comparison of the pressure fluctuations obtained at three angles of attack. Here, the color-map has a logarithmic scale, allowing for a broader comparison of pressure fluctuations. On the left-hand-side, very low values of pressure fluctuations indicate that the flow is steady at $C_L = 0.58$ ($\alpha = 2.755°$). Very small fluctuations can be observed on the shockwave foot, but without any link to a buffet phenomenon. In the center, the pressure fluctuations at $\alpha = 4°$ show that the flow is in buffet conditions. However, contrary to what is observed on the right-hand-side, where $\alpha = 4.25°$, some unsteadiness can be observed in the inner part of the wing, where the so-called "λ shockwave foot" is visible because of the interaction between the wing and the fuselage. The frequencies of the buffet phenomenon observed when $\alpha = 4°$ and $\alpha = 4.25°$ are 11.9 Hz and 12.2 Hz, respectively. These values correspond to a Strouhal number $St = 0.464$, in fair agreement with what was found by Paladini et al. [13] on a similar configuration, where the Strouhal number based on the mean aerodynamic chord for the FLIRET geometry (a half wing-body configuration) was $St = 0.48$.

3. INVESTIGATION AND EVOLUTION OF FAR-FIELD DRAG COMPONENTS OVER A PERIOD

The present section is dedicated to a deeper phenomenological analysis of the unsteadiness entailed by the buffet and its impact on the level of viscous, wave and lift-induced drag over time. The results have been obtained by post-processing the CFD solutions at $M_\infty = 0.85$, $\alpha = 4.25°$, $Re = 20$ million of the Medium grid with the ONERA FFD72 and FFDπ far-field drag analysis codes. First of all, it is necessary to investigate the effect of the size of the integration domain on the various drag components. To do so, the viscous, shock and induced volumes are extended in the wake of the aircraft wing, between $x_W = 50$ m and $x_W = 60$ m (see Fig. 7).

In Fig. 8 and Tab. 1 (top rows), each value is obtained

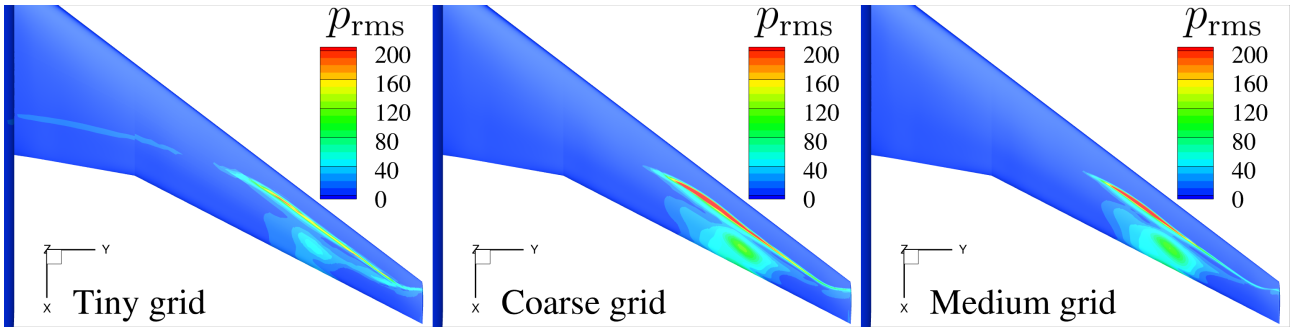

Figure 4: Pressure fluctuations (linear colormap) for different grids.

by performing a time average of the corresponding unsteady drag coefficient over the buffet period. The unsteady coefficients themselves are computed using the unsteady far-field formulation presented in Section 1. On the contrary, the last row of Tab. 1 refers to a steady far-field drag decomposition [3] of the average in time of the flow solutions, also obtained over the buffet period. First, the evolution of the average contribution of each unsteady drag component with respect to x_W is analyzed. In Fig. 8, the time-averaged value for $x_W = 50$ m is subtracted in order to better highlight the relative evolution of each component. In Tab. 1, the exact value for each x_W position can be retrieved. Note that the average of the unsteady far-field drag coefficient $C_{D_{ff}}$ can also be retrieved by Eq. (12) (having $D_m = 0$), and the average of the unsteady near-field drag coefficient $C_{D_{nf}}$ by adding $C_{D_{sp}}$ to $C_{D_{ff}}$. It is shown that the time-averaged unsteady lift-induced drag coefficient C_{D_i} decreases by 5 to 6 counts in favor of the time-averaged unsteady viscous drag coefficient C_{D_v}, which increases by 6 to 7 points as the integration volumes extend in the wing wake. This is the consequence of physical viscous diffusion and of numerical dissipation effects, the latter being likely accentuated by the rapid coarsening of the O-grid in the wake region, which also limits the downstream x_W position allowing to reduce as much as possible the effect of numerical dissipation. On the contrary, the averaged unsteady wave drag coefficient C_{D_w} remains constant at a rather significant level (around 90 counts), while the time-averaged acoustic propagation drag $C_{D_{pa}}$ has a practically negligible contribution to overall drag. It is also interesting to note that the steady drag decomposition of the time-averaged solution is very close to the time-averaged unsteady drag decomposition obtained at $x_W = 50$ m: in the present case, it is because the unsteadiness entailed by the buffet phenomenon is very mild. Nevertheless, Toubin [17] clearly demonstrated that values of steady drag decompositions applied to time-averaged flow solutions can be strikingly imprecise with respect to averaged values of unsteady drag decompositions.

At this stage, it should be pointed out that, in Fig. 7, there are some cells in the wake which are located in between the viscous and shock volumes, but do not belong to either of them. Yet, the wake of the shockwave is to be gradually entrained into the wake of the boundary layer, therefore those untagged cells are not expected. In fact, the extensions of the viscous and shock volumes are defined here using a physical sensor based on the level of viscous stresses and the vorticity modulus, but the latter is dissipated by the rapid coarsening of the grid. Hence,

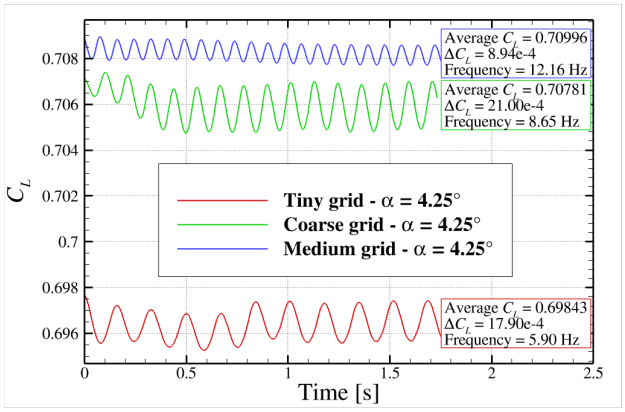

Figure 5: Lift coefficient versus time for different grids.

x_W (in m)	C_{D_i}	C_{D_v}	C_{D_w}	$C_{D_{pa}}$	$C_{D_{sp}}$
Time-averaged drag - Unsteady formulation					
50	200.57	216.78	89.28	0.00	-0.23
52	199.89	218.01	89.27	0.00	-0.77
54	198.86	219.65	89.26	0.01	-1.38
56	197.54	221.28	89.26	0.02	-1.69
58	196.30	222.59	89.26	0.02	-1.76
60	195.35	223.66	89.27	0.01	-1.90
Time-averaged solution - Steady formulation					
–	201.40	215.96	89.02	–	0.03

Table 1: Time-averaged value of each drag component (in counts, i.e. 10^{-4}) for $x_W \in [50\text{ m},\ 60\text{ m}]$ and drag breakdown of the time-averaged solution.

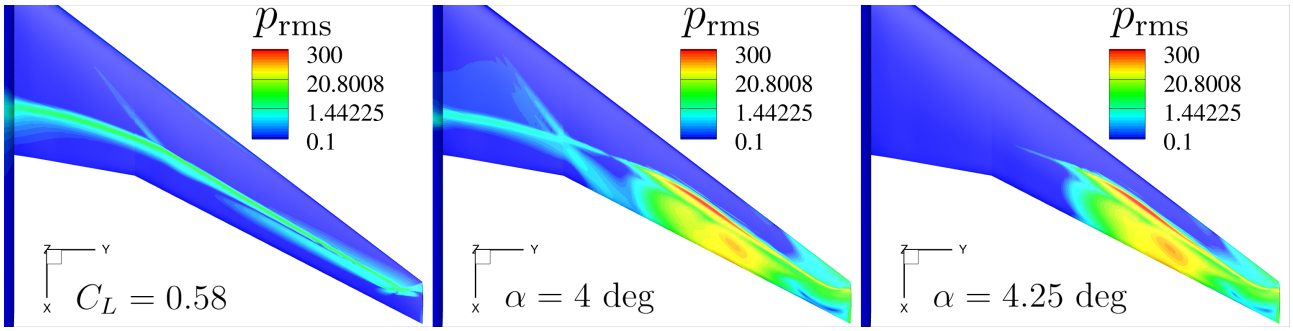

Figure 6: Pressure fluctuations (logarithmic colormap) for different wing loadings at the Medium grid level.

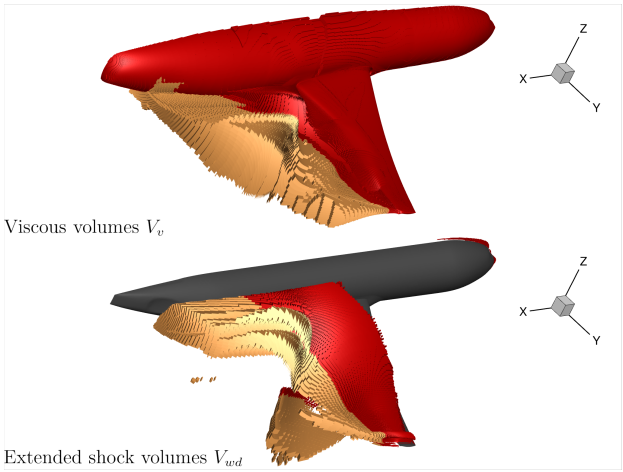

Figure 7: Extension of the viscous and shock volumes for $x_W = 50$ m (in red) and $x_W = 60$ m (in orange) respectively.

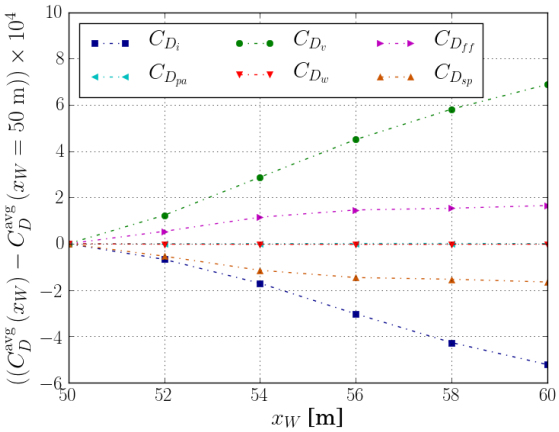

Figure 8: Relative evolution of each drag component averaged in time by the extension of the integration volumes in the wake.

the integration volume issue might be solved by reducing the vorticity threshold used in this criterion. This would lead to the same total far-field drag, but to an eventually slightly different drag decomposition. Besides, some cells below the viscous volume are detected as part of the extended shock volume. There is no shockwave on the pressure side of the wing, therefore this feature is not expected either. Here, increasing the entropy threshold would likely remove those cells from this volume, although their contribution to the overall wave drag value is expected to be small.

An important following step is to verify that the evolution of the far-field drag versus time is synchronized with that of the near-field drag at each time step. In other terms, it consists in checking that the far-field and near-field drag forces are in phase. For this purpose, the evolution of far-field drag versus time has been plotted for all x_W positions and compared to the evolution of near-field drag (see Fig. 9). It is clear that far-field and near-field drag are in phase for all x_W positions, which confirms the consistency of the far-field drag computed by the formulation of Toubin et al. [19]. Regarding viscous and wave drag, the sensitivity of their phase with respect to x_W is plotted in Figs. 10 and 11: for the viscous drag a slight phase shift is observed (perhaps linked to the presence of cells not belonging to either the viscous or shock volume), while for the wave drag all curves are in phase. However, the C_{D_v} curves corresponding to the two most downstream positions $x_W = 58$ m and $x_W = 60$ m show almost no phase shift. In Fig. 12, the phase shift of the unsteady induced drag D_{ui} seems slightly more pronounced than for the viscous drag, although it remains reasonably small. On the contrary, the phase shift becomes even more visible for the lift-induced drag D_i (see Fig. 13). Actually, D_i is computed from D_{ui} after having distinguished the acoustic effects materialized by R^+ and involved in D_{pa}. This phase shift in D_i is indeed directly caused by the great sensitivity of the phase of D_{pa} with respect to x_W (see Fig. 14): although its variation is of a very low amplitude and therefore has a minimal contribution to total drag, it still has a direct impact on the phase of its counterpart D_i. Similarly to the present case, Toubin [17] also observed such a phase shift on D_i for the two-dimensional buffet case over the OAT15A airfoil but

noticed that the phase shift tends to zero when integrating even further in the wake. The author explained that this is caused by a drastic decrease of the contribution of D_{pa}, an effect which is clearly depicted in Fig. 14 for the present case. A gradual decrease in the magnitude of the dephasing D_{pa} contribution would thus lead to a reciprocal decrease in the phase shift of D_i (visible between the $x_w = 58$ m and $x_w = 60$ m curves in Fig. 13). Despite this observation, the choice of a sufficiently downstream x_W position to force the invariance of the phase of D_i is not satisfactory (at least in the present case), due to the influence of numerical dissipation in the wake in lift-induced drag prediction (cf. above disussion). Hence, the $x_W = 50$ m position was chosen for the following analyses in order to ensure, as much as possible, that the computed viscous drag represents the outcome of viscous phenomena occurring on the wing, rather than that of numerical dissipation in the wing wake region.

As shown in Fig. 15, the maximum in viscous drag corresponds to a minimum in wave drag, which is consistent with Toubin's results in the case of two-dimensional buffet [17]. In a two-dimensional buffet case, the wave drag is minimum when the shockwave strength is the weakest, i.e. when the stall cell created by the boundary layer separation downstream of the shockwave foot pushes the shockwave itself at its most upstream buffeting position. This corresponds to the instant when the stall cell reaches its maximum size, hence producing maximum viscous pressure drag D_{vp} (the part of the viscous drag that is not caused by skin friction). The interpretation is however more complex in the current three-dimensional buffet case, because the shockwave oscillates both in the chordwise and the spanwise directions, behaving similarly to a wave propagating towards the wingtip. This is better illustrated in Figs. 16 and 17. At $t = t_2$, the shockwave at the $y = 20$ m section (see Fig. 2) reaches its downstream limit while the shockwave at the $y = 22.5$ m section reaches its upstream limit. The maximum wave drag at $t = t_1$ could be explained by the fact that the shockwave at the $y = 22.5$ m section is at its most downstream position and overcompensates the contribution of the $y = 20$ m section, where the shockwave is at its most upstream position.

Figs. 18, 19 and 20 respectively display approximate spanwise distributions of the wave and viscous pressure drag coefficients C_{D_w} and $C_{D_{vp}}$ computed by the ONERA FFDπ software at $t = t_1$, $t \approx (t_1 + t_2)/2$ and $t = t_2$, comprising a fine discretization in the spanwise direction. The symbols correspond to the time-average of the spanwise distributions and is shown in order to highlight the deviation of the unsteady distribution. A contour of negative streamwise skin friction coefficient C_{f_x} on the wing suction side is also added on each figure in order to visualize the temporal evolution of the size of the separation region caused by the shockwave, allowing to correlate the unsteady flow field variation on the wing to phenomenological drag sources. On average, the presence of the separation region entails a drastic increase in the viscous pressure drag between $y = 10$ m and $y = 22.5$ m. This also coincides with the region of the wing where the wave drag generation is highest. Indeed, the shockwave is strongest around $y = 12$ m, where the flow starts separating downstream. An investigation of the same figures illustrates the convection of the stall cell towards the tip of the wing by the displacement of a region of negative streamwise skin friction. This region matches the displacement of the peak in the spanwise distribution of $C_{D_{vp}}$. This peak in $C_{D_{vp}}$ is very closely preceded by a dip in the spanwise distribution of C_{D_w}. The imperfect synchronization between the peak in $\mathrm{d}C_{D_{vp}}/\mathrm{d}y$ and the dip in $\mathrm{d}C_{D_w}/\mathrm{d}y$ is likely related to the very slight phase shift between the maximum reached by $C_{D_{vp}}$ and the minimum reached by C_{D_w} illustrated in Fig. 15.

CONCLUSION

In the present study, the unsteady far-field drag decomposition method developed by Toubin et al. [19] has been adapted to a single-vector formulation and applied to the three-dimensional transonic buffet phenomenon over the NASA Common Research Model. To the authors' knowledge, this constitutes the first attempt at decomposing the drag in three-dimensional buffet conditions using a far-field technique.

The flight conditions investigated in this study enabled to effectively observe the onset of a very mild buffet phenomenon where the unsteadiness was confined to a region of limited size on the wing suction side. The Strouhal number of the observed buffet phenomenon appeared to be in line with previous results from the literature. In spite of this unsteadiness being very mild, the unsteady far-field drag decomposition method could capture the oscillations in the wave, viscous and lift-induced drag exerted on the aircraft. It was observed that the wave drag was maximum when the viscous drag was minimum and *vice versa*, as it was previously shown by Toubin et al. [19] in two space dimensions. Sensitivity analyses of the phase shift with respect to the wake extension of the integration volumes were also proposed, suggesting that the phase of the wave drag and the viscous drag is almost insensitive to this parameter, whereas the phase of the lift-induced drag showed a more pronounced sensitivity to the investigated integration volume wake boundaries, as these limits remained rather close to the wing.

In the end, some local analyses were carried out with the aim to link the unsteady variation of drag components to flow field variations. It was observed that the convection of the stall cell and the oscillation of the shockwave on the wing suction side are well depicted on the intensity of unsteady spanwise generation of wave and viscous

pressure drag. The stall cell is characterized by a bump in the viscous pressure drag distribution and a dip in the wave drag distribution, whereas the shock oscillation is merely translated into oscillations on both distributions.

In the future, further investigations will be conducted with the aim to perform grid convergence studies. Then, potential improvements to physical sensors can be made (essentially the threshold robustness). Finally, additionnal simulations (URANS and/or ZDES) and drag analyses on a stronger buffet case can be carried out.

ACKNOWLEDGEMENTS

The studies presented have used the elsA software, whose development is partially funded by its two co-owners: ONERA and SAFRAN.

The authors are grateful to Didier Bailly, ONERA, for the fruitful discussions on the unsteady far-field drag decomposition and to David Hue, ONERA, for his suggestions and for providing the steady flow solutions on the NASA CRM, from which the unsteady computations were restarted.

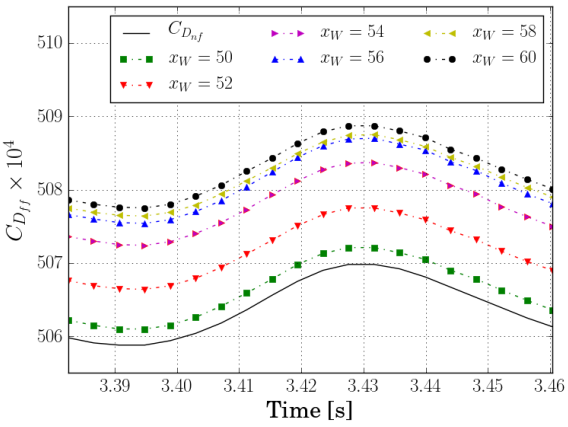

Figure 9: Temporal evolution of the far-field drag versus the near-field drag for various x_W positions.

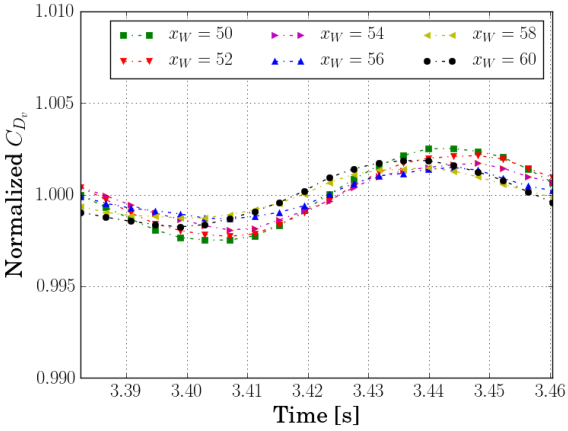

Figure 10: Temporal evolution of the viscous drag normalized by the time-averaged value for various x_W positions.

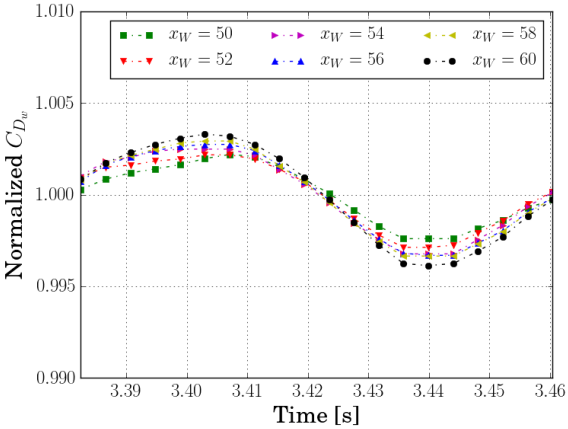

Figure 11: Temporal evolution of the wave drag normalized by the time-averaged value for various x_W positions.

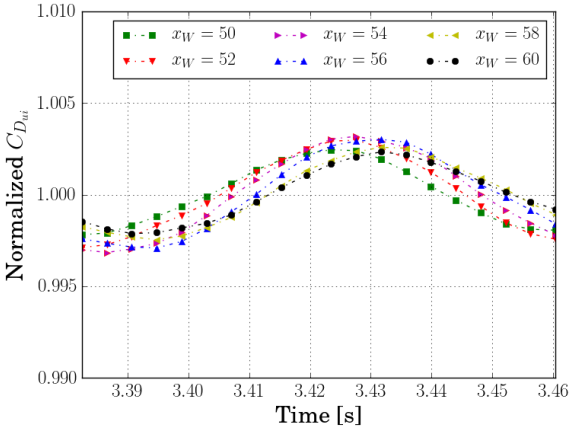

Figure 12: Temporal evolution of the unsteady induced drag normalized by the time-averaged value for various x_W positions.

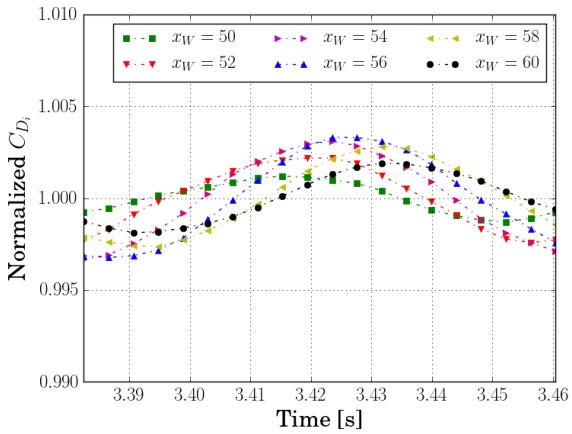

Figure 13: Temporal evolution of the lift-induced drag for various x_W positions.

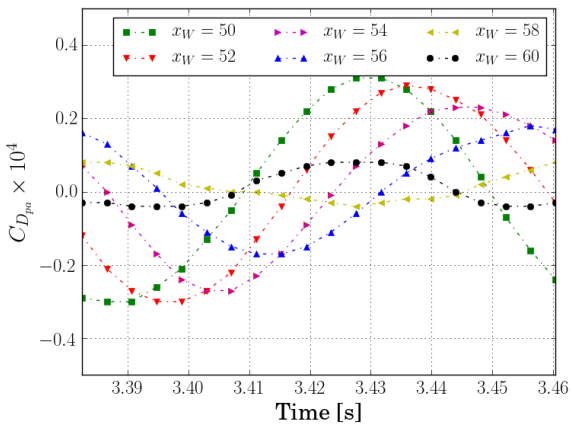

Figure 14: Temporal evolution of the acoustic propagation drag for various x_W positions.

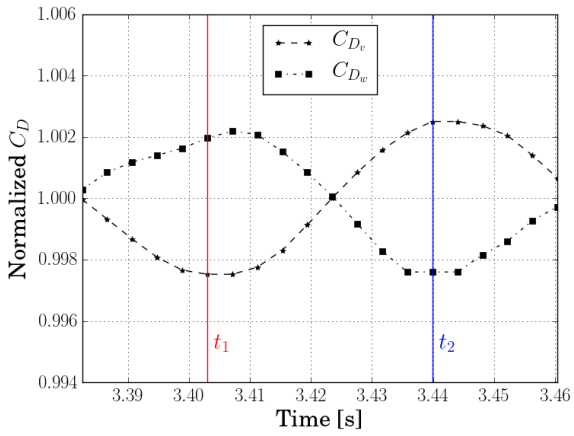

Figure 15: Temporal evolution of C_{D_v} and C_{D_w} (normalized by their average in time) at $x_W = 50$ m.

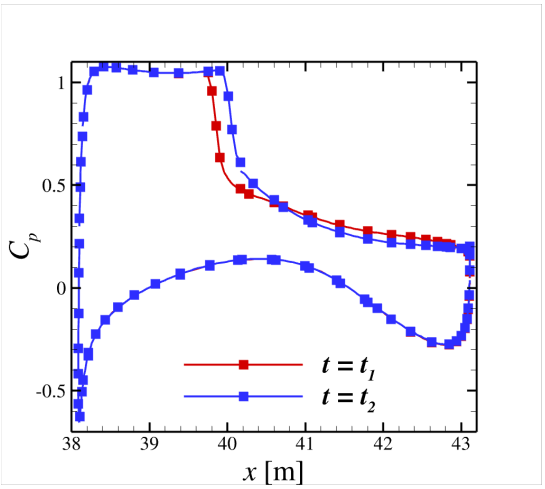

Figure 16: Pressure coefficient at spanwise station $y = 20$ m for $t = t_1$ and $t = t_2$.

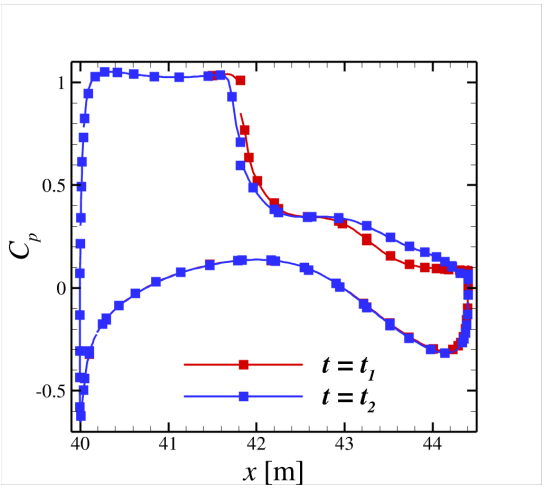

Figure 17: Pressure coefficient at spanwise station $y = 22.5$ m for $t = t_1$ and $t = t_2$.

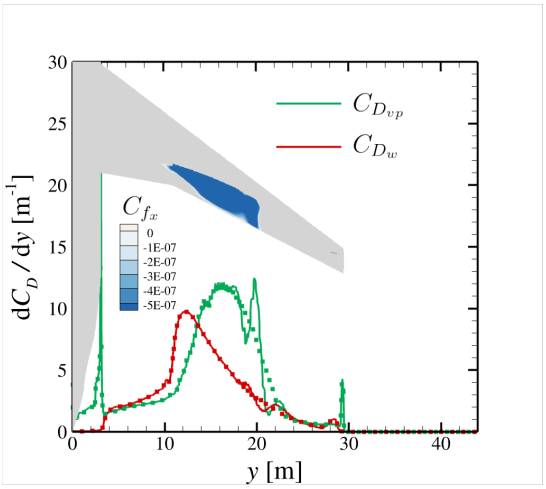

Figure 18: Spanwise distributions of $C_{D_{vp}}$ and C_{D_w} for $t = t_1$.

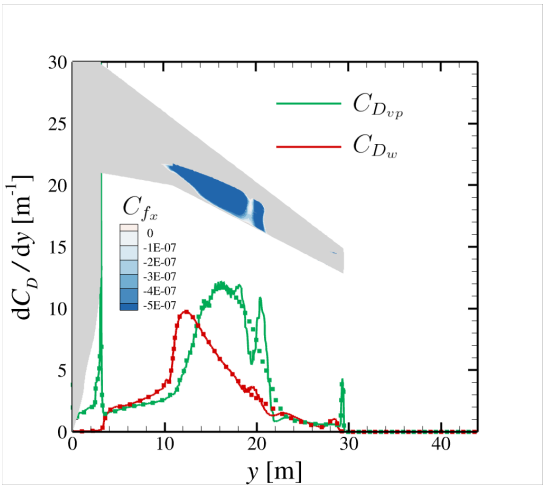

Figure 19: Spanwise distributions of $C_{D_{vp}}$ and C_{D_w} for $t \approx (t_1 + t_2)/2$.

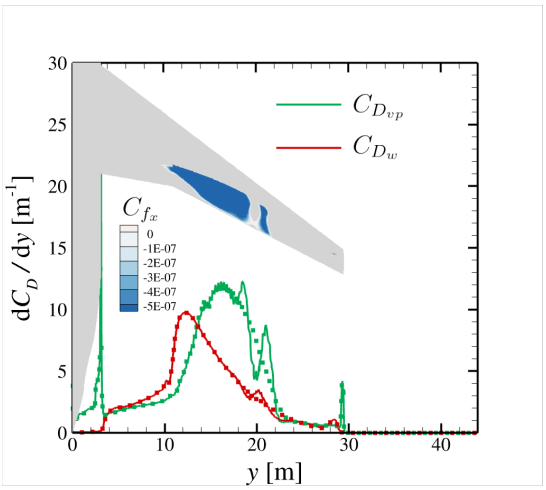

Figure 20: Spanwise distributions of $C_{D_{vp}}$ and C_{D_w} for $t = t_2$.

REFERENCES

[1] L. Cambier, S. Heib, and S. Plot. The ONERA elsA CFD software: input from research and feedback from industry. *Mechanics & Industry*, 14(3):159–174, 2013.

[2] J. G. Coder, D. Hue, T. H. Pulliam, A. J. Sclafani, L. Serrano, and J. C. Vassberg. Contributions to the sixth drag prediction workshop using structured, overset grid methods. *Journal of Aircraft*, 55(4):1406–1419, 2018.

[3] D. Destarac. Far-field/near-field drag balance and applications of drag extraction in CFD. *VKI Lecture Series*, 2:3–7, 2003.

[4] D. Destarac and J. van der Vooren. Drag/thrust analysis of jet-propelled transonic transport aircraft; definition of physical drag components. *Aerospace Science and Technology*, 8(6):545–556, 2004.

[5] M. Gariépy, J.-Y. Trépanier, and B. Malouin. Generalization of the far-field drag decomposition method to unsteady flows. *AIAA Journal*, 51(6):1309–1319, 2013.

[6] D. Hue, F. Sartor, I. Petropoulos, and C. Fournis. Steady and unsteady computations of the CRM aircraft at different Reynolds numbers. *Journal of Aircraft*, submitted and currently under review.

[7] A. Jameson, W. Schmidt, and E. Turkel. Numerical solution of the Euler equations by finite volume methods using Runge Kutta time stepping schemes. In *14th Fluid and Plasma Dynamics Conference*, Paper 81-1259, 1981.

[8] B. H. K. Lee. Self-sustained shock oscillations on airfoils at transonic speeds. *Progress in Aerospace Sciences*, 37(2):147–196, 2001.

[9] E. C. Maskell. Progress towards a method for the measurement of the components of the drag of a wing of finite span. Technical Report 72232, Procurement Executive, Ministry of Defence, Royal Aircraft Establishment, 1972.

[10] M. Ostieri, B. Mele, and R. Tognaccini. Linear and nonlinear decomposition of aerodynamic force acting on an oscillating plate. *AIAA Journal*, 56(2):594–608, 2018.

[11] M. Ostieri, R. Tognaccini, D. Bailly, and D. Destarac. Aerodynamic force and Lamb vector field in compressible unsteady flows. In *2018 AIAA Aerospace Sciences Meeting*, Paper 2018-0548, 2018.

[12] K. Oswatitsch. *Der luftwiderstand als integral des entropiestromes*. Vandenhoeck & Ruprecht, 1945.

[13] E. Paladini, J. Dandois, D. Sipp, and J.-C. Robinet. Analysis and comparison of transonic buffet phenomenon over several three-dimensional wings. *AIAA Journal*, 57(1):379–396, 2019.

[14] L. Prandtl. Theory of lifting surfaces. Technical Report NACA TN10, National Advisory Committee for Aeronautics, 1919.

[15] P. Spalart and S. Allmaras. A one-equation turbulence model for aerodynamic flows. In *30th Aerospace Sciences Meeting and Exhibit*, Paper 1992-439, 1992.

[16] E. N. Tinoco, O. P. Brodersen, S. Keye, K. R. Laflin, E. Feltrop, J. C. Vassberg, M. Mani, B. Rider, R. A. Wahls, J. H. Morrison, et al. Summary data from the sixth AIAA CFD drag prediction workshop: CRM cases. *Journal of Aircraft*, 55(4):1352–1379, 2018.

[17] H. Toubin. *Prediction and phenomenological breakdown of drag for unsteady flows*. PhD thesis, Université Pierre et Marie Curie, 2015.

[18] H. Toubin and D. Bailly. Development and application of a new unsteady far-field drag decomposition method. *AIAA Journal*, 53(11):3414–3429, 2015.

[19] H. Toubin, D. Bailly, and M. Costes. Improved unsteady far-field drag breakdown method and application to complex cases. *AIAA Journal*, 54(6):1907–1921, 2016.

[20] J. van Der Vooren and J. W. Slooff. CFD-based drag prediction: state-of-the-art, theory, prospects. *National Aerospace Lab., NLR, TP 90247 U*, 1992.